RESEARCH ARTICLE

ADVANCED
PHYSICS
RESEARCH
Open Access

www.advphysicsres.com

Electrical Effects of Ionic Deficient Cubic Ferrite Spinels: A Case Study on MgFe₂O₄

*Farshad Farshidfar, Hannah Oreskovic, Dominic H. Ryan, and Khashayar Ghandi**

Electron transport via indirect exchange interactions between octahedral sites in spinels is affected by cationic or anionic vacancies. Thus, the deviation of the electron hopping mechanism is investigated, from a constant energy barrier toward a variable range energy barrier in iron-deficient and oxygen-deficient cubic magnesium ferrite spinels. Variable range electron hopping activation energy at high temperatures is consistent with the modified cation–anion interactions in the distorted structure of an ionic deficient cubic magnesium ferrite spinel. For these observations, an instrumental method is developed to evaluate the electron exchange interactions and general redox kinetics on surfaces, managed by exposure to the flow of a wide variety of desired gases. The applications of this instrument are far beyond the example studies reported here.

1. Introduction

The ability to study the electro-thermal and in situ surface reactivity of ceramics has many applications in catalysis and semiconductor industries. This paper describes the development of such measurements with examples of applications to ferrite spinels, which are of the form MFe_2O_4, where M is a cation with an oxidation state of two. This is an important class of ferrimagnetic spinels[1] and has broad applications in electrocatalysis,[2,3] photocatalysis,[4] chemical sensing,[5,6] hyperthermia,[7] electromagnetic devices,[8] and stress or force sensing.[9] The unit cell of a non-defective ferrite spinel is composed of 24 cations and 32 oxygen anions arranged in a face-centered cubic (FCC) structure, of the Fd3m space group. To avoid deviation from cubic structure, M should not be a Jahn–Teller-active cation. In MFe_2O_4 ferrite spinels, M^{2+} and Fe^{3+} are distributed among available interstitial sites including 8 out of 64 tetrahedral sites, denoted by curved brackets, and 16 out of 32 octahedral sites, denoted by square brackets. Hence, ferrite spinels can be formulated as $(M_{1-\alpha}Fe_\alpha)[M_\alpha Fe_{2-\alpha}]O_4$, where α is the inversion degree. An α of 0 indicates normal spinel while an α of 1 indicates an inversed spinel. Any value of α between 0 and 1 indicates a mixed spinel.[10–12]

Magnesium ferrite spinel, shown as $MgFe_2O_4$, is a 2–3 class of spinel, meaning the oxidation state for Mg is divalent and for Fe is trivalent. Thermal diffusion of iron and magnesium cations is the main mechanism proposed for the formation of $MgFe_2O_4$ from Fe_2O_3 and MgO.[13] In any form of cation distribution, the octahedral sites of $MgFe_2O_4$ spinels are occupied by iron cations, which play a crucial role in the electrical and magnetic properties of spinels.[14] Additionally, octahedral sites share their edges as shown in **Figure 1**. Coupling of the spins of Fe-d orbital electrons at octahedral sites occurs via a double exchange interaction mechanism through two shared oxygens with an Fe—O—Fe angle of $\approx 90°$.[15] Octahedral sites share their corners with tetrahedral sites and the electron spin coupling of Fe-d orbitals occurs via a superexchange interaction with a wide Fe-O-Fe angle of $\approx 180°$.[15] Another factor is the double exchange interaction, which leads to the parallel electron spin orientation of Fe-3d orbitals at octahedral sites and the antiparallel spin orientation of Fe-3d orbitals among tetrahedral and octahedral sites, as illustrated in Figure 1.[16,17]

Electrons that are generated by oxygen vacancies play the main role in forming Fe^{3+}/Fe^{2+} pairs in the spinel structure.[18,19] $MgFe_2O_4$ behaves as an n-type semiconductor and electron transfer is described by the electron hopping mechanism between 3d orbitals of iron cations in different oxidation states, based on converting $[Fe^{2+}]$-O-$[Fe^{3+}]$ to $[Fe^{3+}]$-O-$[Fe^{2+}]$.[5,20] Electrons do not hop via superexchange interactions of $[Fe^{2+}]$-O-(Fe^{3+}) because of antiparallel spin configurations. Electron hopping between tetrahedral sites does not occur as they lack shared oxygen and have a long hopping distance. They instead hop via a double exchange interaction mechanism through octahedral chains because of parallel spin configuration.[21,22]

The cation–anion interaction at the octahedral site is related to the spatial orbital overlap of Fe 3d and O 2p, which depends on the cation–anion distance. Stronger orbital overlap enhances electron exchange interactions.[14] Oxygen displacement from the ideal position, by structural distortion, affects the degree of orbital overlap. This overlap depends on the position of the

F. Farshidfar, H. Oreskovic, K. Ghandi
Department of Chemistry
University of Guelph
Guelph, ON N1G 2W1, Canada
E-mail: kghandi@uoguelph.ca
D. H. Ryan
Physics Department
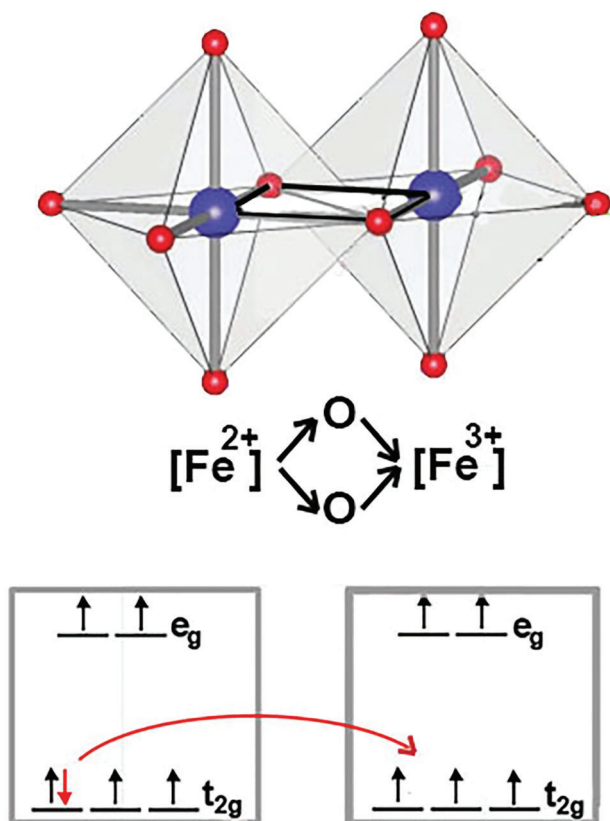McGill University
Montreal H3A 2T8, Canada

Figure 1. Electron hopping between Fe cations of different oxidation states, at two adjacent octahedral sites, via a double exchange interaction mechanism through edge-sharing oxygens. Fe cations are blue and O anions are red.

oxygen anions, represented as the oxygen parameter (u), which is 0.250 for the non-distorted and ideal octahedral site.[12,23] Higher values of u represent the increasing volume of the tetrahedral site that accompanies decreasing the volume of the octahedral site.[24] The value of u shifts to fit the cations at interstitial sites according to their ionic radii.[12,24,25]

A novel in-house, atmospheric-controlled flow mode conductivity instrument is utilized here to demonstrate the ionic deficiency of $MgFe_2O_4$, as a continuation of our previous study on its oxidation kinetics, where a rate constant of $1.867(7) \times 10^{-5}$ s^{-1} was measured via electrical conductivity.[25] Deficiencies of ferrite spinel in this study are defined by missing iron as a cation or oxygen as an anion both of which contribute to the electron transport. The impact of ionic deficiency in $MgFe_2O_4$ spinels, in the forms of both cationic and anionic deficiencies, on the mechanism of electron hopping, was established using this novel instrumental approach that is detailed in Sections 2.1 and 2.2.

2. Experimental Section

2.1. Sample Preparation

To prepare the $MgFe_2O_4$ spinel, the standard co-precipitation method was used with analytical grade $Mg(NO_3)_2 \cdot 6H_2O$ (Sigma–Aldrich, ACS reagent 99%) and $Fe(NO_3)_3 \cdot 9H_2O$ (Sigma–Aldrich,

ACS reagent, >98%) as starting materials. The precipitation agent was analytical grade NaOH (Sigma–Aldrich, >98%). Powders were pressed to form pellets, followed by a 3 h firing process at 850 °C, in a controlled atmosphere, to form the spinel structure. Calcined samples in air and nitrogen were denoted as MFA and MFN respectively.

Square-shaped samples (10 mm x 6 mm x 1 mm) were prepared by polishing pellets after the calcination process. Electrical resistance was simply measured between two contacts (2 mm x 6 mm) applied by silver paste (Sigma–Aldrich, 200 nm 80%) on either side of one face of the pellets. To study the effect of the atmosphere on the electrical properties of MFA and MFN, prepared pellets were reduced through heat treating at 250 °C in ultra-pure grade N_2 for 2 weeks, followed by 250 °C exposure to ultra-pure grade air, called Zero-Air, as the oxidizing gas. In the study described in this report, electrical conductivity was measured for each gas treatment in situ and in the flow mode to evaluate the impact of ionic deficiencies on electron hopping behavior. The process is summarized in **Figure 2**.

2.2. Electrical Conductivity Cell

An in-house electrical conductivity instrument was designed to be used for redox kinetics studies (the previous report) and to evaluate electrical properties as shown in **Figure 3**. The instrument can be used for studies under a wide range of temperatures from liquid nitrogen temperature up to 400 °C and even up to 800 °C with the most recent modifications. However, for the studies detailed in this report, the measurements were done in the temperature range of 150–250 °C (423–523 K). In this design (Figure 3), the sample was placed between two copper plates that were electrically in contact with two spring-loaded pins. A 40 W heater was placed just above the sample, without touching it. Steel tubes were of dual function; they contained gas flow in/out and they guided the k-type thermocouple, adjusted between sample and heater near the sample, without touching it. The cell was equipped with two thermocouples, one to adjust the temperature and the other to record the temperature of the cell. Ultra-high purity Alumina (99.8%) was used as an insulating sample holder, where electrical conductivity should be avoided. The two-contact measuring method of electrical resistance was carried out in both directions by switching the contacts of the probes of an electronic voltmeter (Fluke, Model 117 Root Mean Square). The averages of the two values were measured by switching the probes at predetermined temperatures.

The electrical conductivity was reported by $\sigma = d/R \bullet A$ in S cm^{-1}, where R was resistance in Ω, d was the sample thickness in cm and A was the area between electrical contacts in cm^2. The previous report[26] explained the details of the circuits used to record the resistance and temperature for kinetic studies.

2.2.1. Additional Instrument Options

The cell had a cooling component attached to the bottom of the cell (**Figure 4**). Its cooling mechanism was based on the circulation of any coolant using regular lab chillers or liquified gases such as liquid nitrogen. Such a feature enabled the measurement of electrical properties below 0 °C.
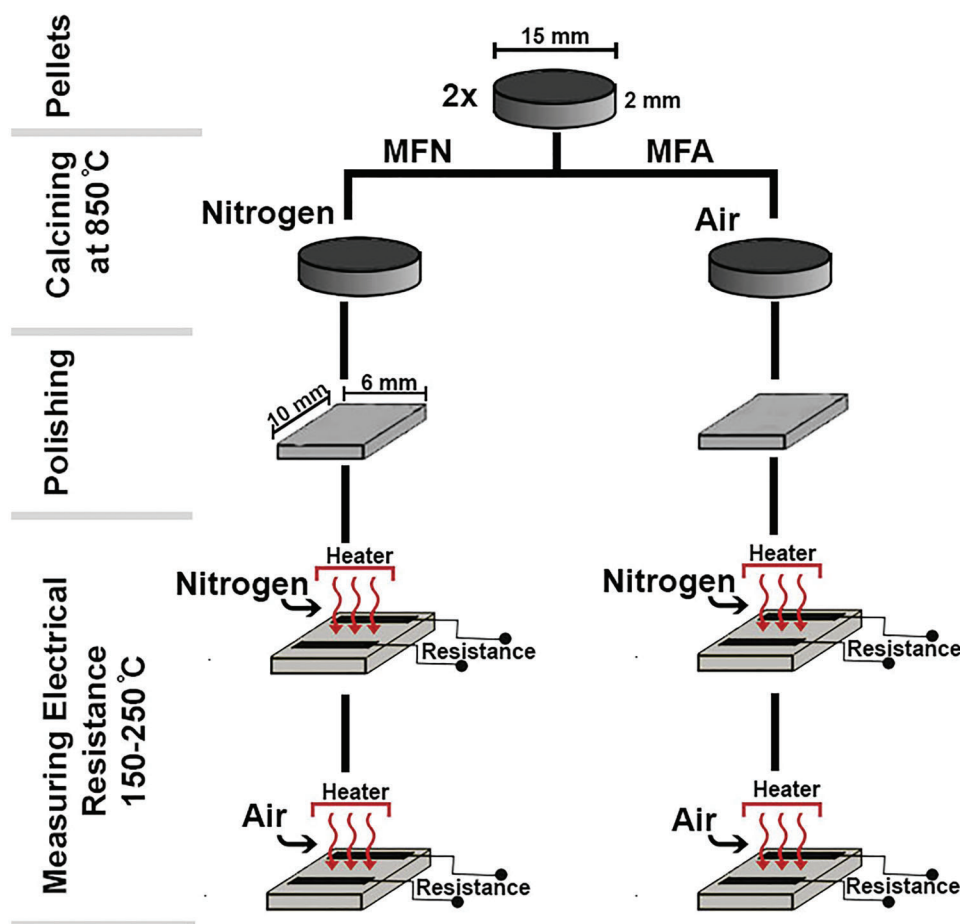
**ADVANCED
SCIENCE NEWS**

www.advancedsciencenews.com

**ADVANCED
PHYSICS
RESEARCH**
Open Access

www.advphysicsres.com

Figure 2. The sample preparation process for the evaluation of gas treatment effects on the structural and electrical properties of $MgFe_2O_4$.

Gas connection points were connected to a larger gas flow network equipped with a mass flow controller. The selected gas can be used for continuous or pulsed exposure to the sample, in sample preparation, or during sample measurements. For additional options, the gas network can be attached to any gas canister or generator, for flexibility in gas selection and gas concentration. For studies of reactive oxygen species, an ozone generator was used (**Figure 5**), like methods used in the previous report to study reactive oxygen species reactions on the surface of ceramics.[34] There was a liquid line in the way to the cell with a T valve that can be used to transform ozone into different reactive oxygen species, which was an important feature for studies of corrosion in situ.

Furthermore, there was another option for experimental variation, with a liquid injection site. Featuring an additional heating system, liquids such as alcohol or water can be injected and vaporized in a chamber with the gas flow, then delivered to the sample accompanying the gas. These abilities to manipulate gas conditions or liquid exposure to the sample were among novelties and further demonstration of the flexibility and thus wide potential use of this instrument. The current-specific cell enabled the precise evaluation of the electron hopping mechanism of the solid-state material while being exposed to any desired gas under a controllable flow mode. This feature was not provided in

regular cells; hence the reduced sample gets reoxidized while measuring the electrical conductivity. As far as it is known,, there was no other commercial instrument available with all the abovementioned features in the market, hence the need to develop this novel system.

2.3. Characterization

Powder x-ray diffraction (PXRD) measurements were performed using a PANalytical Empyrean diffractometer in a reflection (Bragg−Brentano) geometry with a Cu Kα radiation source, a Ni Kβ filter, and a PIXcel1D linear detector. A powdered sample was loaded into a sample holder with a 16 mm insert, which was mounted on a spinning stage at room temperature. Powder diffractograms were recorded in the 5−110° 2θ range with a step size of 0.0131° and an exposure time of 60 s per step. Data was collected and controlled using Data Collector software and smoothed using HighScore Plus (version 4.1). The Rietveld refinement of XRD patterns was carried out by Materials Analysis Using Diffraction (MAUD), version 2.992. The values of the least-squares parameter (R_{wp}) were monitored to evaluate the accuracy of refinement. Debye−Scherrer and Williamson−Hall methods were used to compare

**ADVANCED
SCIENCE NEWS**

www.advancedsciencenews.com

**ADVANCED
PHYSICS
RESEARCH**
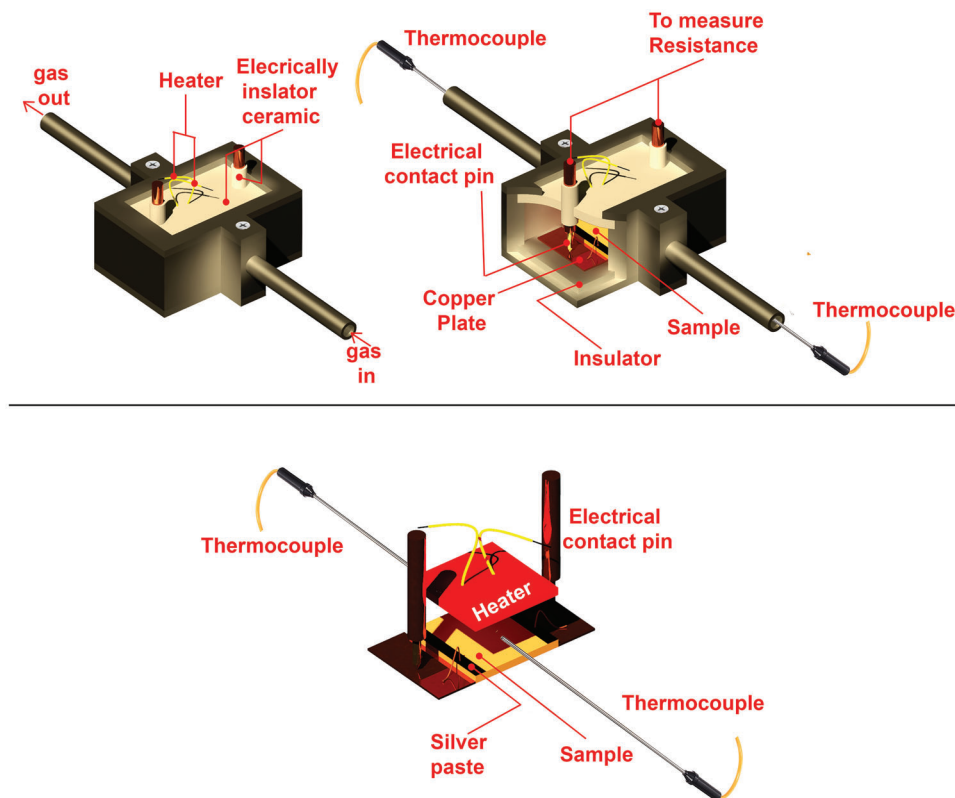Open Access

www.advphysicsres.com

Figure 3. The electrical conductivity cell for the study of redox kinetics and the measurement of electrical resistance, in a controlled atmosphere, in a temperature range of 150–250 °C.[26]
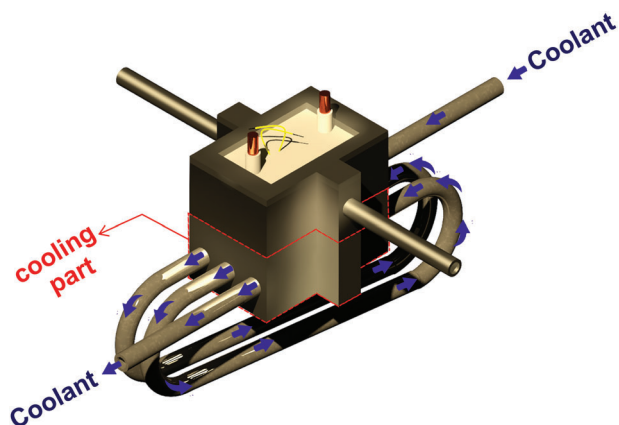

Figure 4. Additional cooling part attached to the bottom of the cell for cooling purposes.

the crystallite size and the strain. The Fourier transform Infared (FTIR) spectra (380 cm^{-1}-4000 cm^{-1}) were collected by compact Bruker (ALPHA II). The room temperature Mössbauer spectra were collected on a conventional constant-acceleration spectrometer that was calibrated using a thin iron-metal foil. Velocity zero was set as the centroid of the calibration spectrum. Before measurements, the samples were hand-ground to a fine powder and mixed with boron nitride to make a uniform absorber.

3. Results and Discussion

According to the x-ray diffraction (XRD) patterns shown in **Figure 6**, MFA is a multiphase material containing 21.7(3) %V (volumetric percentage) of the Fe_2O_3 phase. However, the Fe_2O_3 phase disappeared in MFN when the calcination was carried out in a nitrogen environment. This observation, which was consistent with our Mössbauer data (**Figure 7**), and with the definite reddish color of the MFA when hand-ground (unlike MFN), further supports the presence of a haematite phase in MFA and not in MFN. The XRD data also confirms the formation of a non-stoichiometric Fe-deficient phase of $MgFe_2O_4$ by calcination at 850 °C in air. The formation of $MgFe_2O_4$ is based on counter-cationic diffusion, and Fe_2O_3 remains a secondary phase due to the higher activation energy of Fe^{3+} diffusion over Mg^{2+},[13] leaving the $MgFe_2O_4$ phase Fe-deficient. The secondary phase of Fe_2O_3 is reported in other investigations with similar preparation methods.[18,27]

An oxygen-free calcination environment enhances the formation of $MgFe_2O_4$ at 850 °C with no secondary phase. Elimination of Fe_2O_3 in an oxygen-free calcination atmosphere confirms the enhanced cationic diffusion by the formation of Fe^{2+} with a smaller diffusion activation energy compared to that of Fe^{3+}.[13,28] By switching the calcination environment from air to nitrogen, the Fe_2O_3 phase is eliminated, confirming the formation of monophase $MgFe_2O_4$.

The extra feature appearing outside the leftmost peak of the Mössbauer spectra confirms the secondary phase, which is
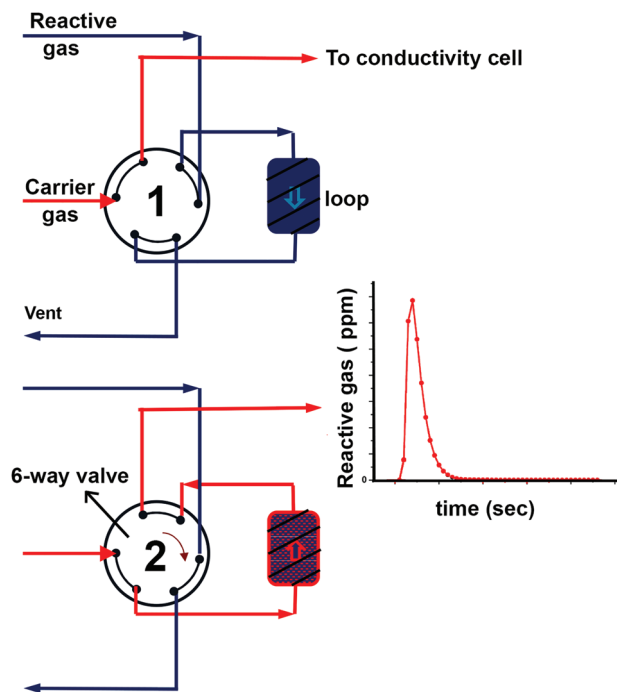
**ADVANCED
SCIENCE NEWS**

www.advancedsciencenews.com

**ADVANCED
PHYSICS
RESEARCH**
Open Access

www.advphysicsres.com

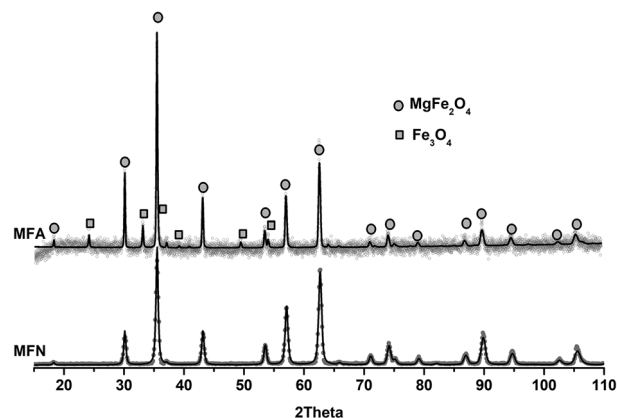**Figure 5.** Reactive gas purging feature with nonreactive carrier gas.

Figure 6. The XRD pattern of MgFe$_2$O$_4$ calcined at 850 °C in air (MFA) and in nitrogen (MFN). Calcined samples in air and nitrogen are denoted as MFA and MFN, respectively.

haematite. This phase disappears with the treatment of the spinel under nitrogen at 850 °C.

The theoretical density is the density of a single crystal, without structural defects. Based on the value of the lattice constant and the types of elements, the theoretical density is calculated as the mass of elements multiplied by the number of atoms in a unit cell/volume of a unit cell to determine x-ray density, which is calculated based on the refined XRD pattern.

The porosity is calculated by $\%P = (1-d_x/d_b)\cdot100$, where d_x is X-ray density and d_b is the observed bulk density. According to the results, porosity has been reduced significantly by an enhanced crystallization process under an oxygen-free calcination environment. MgFe$_2$O$_4$ is further densified by switching the calcination atmosphere from air to nitrogen.
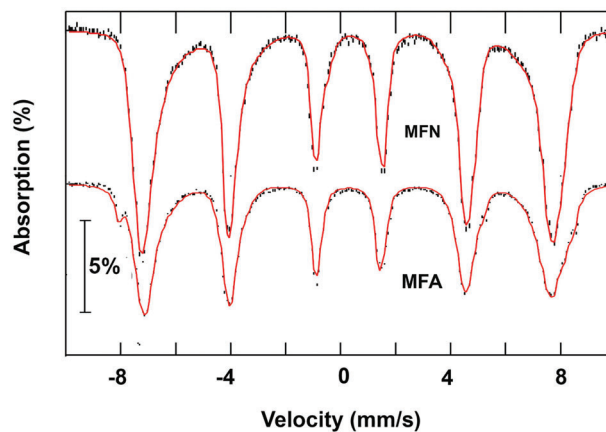

Figure 7. Mössbauer spectra of MgFe$_2$O$_4$ calcined at 850 °C in air (MFA) and in nitrogen (MFN).

Table 1. The structural parameters extracted by evaluating the XRD patterns. a is the lattice parameter, α is the cation distribution extracted by the Bertaut method and Rietveld refinement, u is the oxygen parameter, and I is the peak intensity of the X-ray diffraction pattern.

Sample	a [Å]	α[a]	α[b]	u	$\frac{I_{(400)}}{I_{(422)}}$
MFA	8.397	0.57(9)	0.6(1)	0.254	32
MFN	8.383	0.83(1)	0.9(1)	0.261	16

[a] Bertaut Method; [b] Rietveld refinement.

The ratio of XRD peak intensities related to (400) and (422) Miller indices is used to extract the cation distribution, noted as the inversion degree (α) based on the Bertaut method,[29] and according to Equation (1):

$$\frac{I_{(400)}}{I_{(422)}} = \frac{\left(8\left(-F_{(A)} + 2F_{[B]} + 4F_O\right)\right)^2 P_{400} L_{400}}{\left(8F_{(A)}\right)^2 P_{422} L_{422}} \quad (1)$$

where F, P, and L are structure, multiplicity, and Lorentz polarization factors, respectively.

Based on observations when switching the calcination atmosphere to nitrogen, the inversion degree increases to 0.83, which approaches the preferred cation distribution of MgFe$_2$O$_4$. As reported in **Table 1**, cation distribution (α) extracted from the Bertaut method and Rietveld refinement are in good agreement for both samples. The higher u value of MFN compared to MFA confirms that the oxygen anion shifts from its ideal position. This positional shift occurs toward cations in octahedral sites and originates from the structural distortion generated in an oxygen-free atmosphere. This supports a higher concentration of oxygen vacancies in an oxygen-free calcination environment. As seen in Table 1, the inversion degree of MFA is 0.57, consistent with a random cation distribution of Mg and Fe in both octahedral and tetrahedral sites. However, by switching the calcination atmosphere to nitrogen, the inversion degree increases to 0.83, which approaches the preferred cation distribution of MgFe$_2$O$_4$.

Using the Debye-Scherrer equation, crystallite size is inversely proportional to the full width at half maximum (FWHM). **Figure 8** compares the (311) Miller index diffraction peaks of MFA and MFN adjusted along the x-axis by $\Delta(2\theta) = (2\theta)_{act.}$-
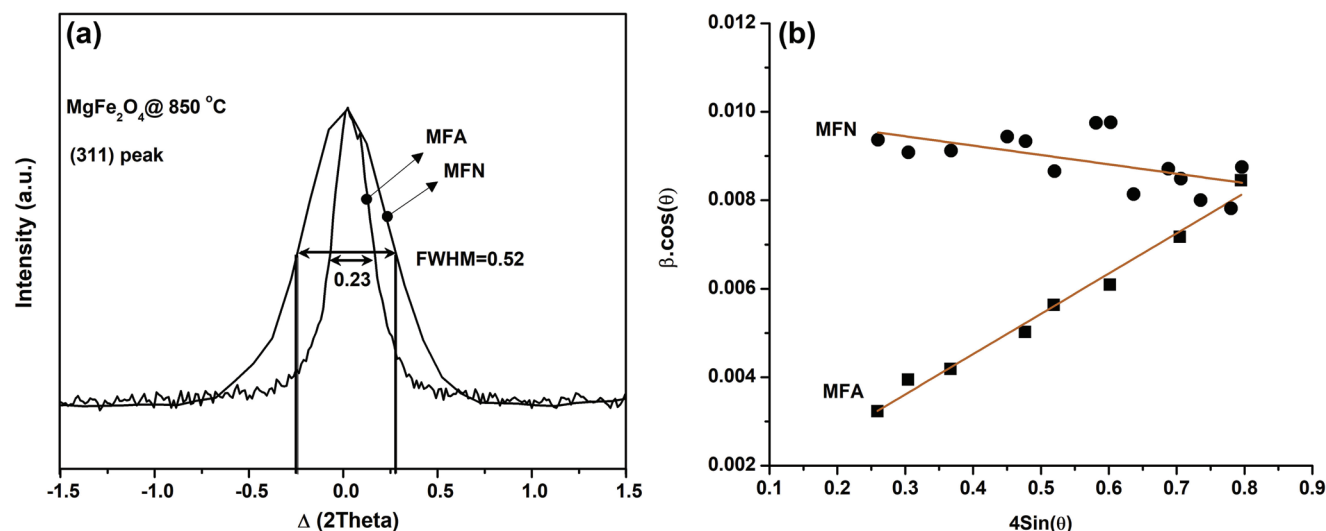
2300057 (5 of 10)

ADVANCED
SCIENCE NEWS

www.advancedsciencenews.com

ADVANCED
PHYSICS
RESEARCH
Open Access

www.advphysicsres.com

Figure 8. a): The full width at half maximum (FWHM) of (311) peak, b): Plot of $\beta\cos(\theta)$ versus $4\sin(\theta)$.

Table 2. Volume and mass fraction of phases based on the XRD pattern refinement (Theo. is the theoretical value and Obs. is the observed value).

Sample	MgFe$_2$O$_4$		Fe$_2$O$_3$		Theo.	Obs.	Porosity	Crystallite size	Strain
	g cm^{-3}	%V.	g cm^{-3}	%V.	g cm^{-3}		%	Nm	$\epsilon \times 10^3$
MFA	4.48	78.3(7)	5.26	21.7(3)	4.65	2.68	42.4(5)	157.6 ± 443	9.11 ± 05
MFN	4.51	100	–	–	4.51	3.54	21.5(2)	13.8 ± 07	−2.12 ± 08

$(2\theta)_{max.}$, where $(2\theta)_{act}$ is the diffraction angle and $(2\theta)_{max.}$ is the angle of diffraction at maximum intensity. The Williamson–Hall method was used where the crystallite size and crystallite strain are extracted by plotting $\beta\cos\theta$ versus $4\sin\theta$, according to the Williamson–Hall Equation (2):

$$\beta \, \cos\theta = \frac{k\lambda}{D} + 4\epsilon \, \sin\theta \tag{2}$$

where β is the full width at half maximum (FWHM), D is the crystallite size, k is the shape factor (0.9), and ϵ is the uniform strain of the crystal. According to the values obtained by applying the Williamson–Hall method, the crystallite size of MgFe$_2$O$_4$ is reduced from 157 ± 44 nm in MFA to 13.8 ± 0.7 nm in MFN. This is inconsistent with the homogenous growth of crystals due to the enhanced mobility of cations in oxygen-deficient ferrite spinels. Switching the calcination atmosphere from air to nitrogen affects the strain as well. According to the strain calculated by the Williamson–Hall method and summarized in **Table 2**, the nitrogen environment shifts the internal strain to a negative value, which supports the impact of oxygen deficiency on the crystal's negative strain.

The expanded structure of magnesium ferrite spinels calcined under air is obvious by its higher lattice parameters and the cation-cation distances, including (A)-(A), [B]-[B], and (A)-[B]. The [B]-O distance in the octahedral site is reduced from 2.068 to 2.005 Å in an oxygen-free calcination environment. This confirms the stronger orbital overlap at octahedral sites due to distorted spinel structure (**Table 3**).

Table 3. Cation-cation and cation–anion distance extracted from the Rietveld refinement.

Sample	R_{wp}	(A)-(A)	[B]-[B]	(A)-[B]	(A)-O	[B]-O
				Å		
MFA	0.03	3.636	2.969	3.481	1.873	2.068
MFN	0.24	3.629	2.963	3.473	1.979	2.005

(A) = Tetragonal & [B] = Octahedral in (A)[B]$_2$O$_4$ spinel structure; $d_{(A)-O} = a(u-1/8)\sqrt{3}$ & $d_{[B]-O} = a\sqrt{(3u^2-2u+3/8)}$ where d is the distance in Å, u is the oxygen parameter, and a is the lattice parameter.

The FTIR spectra show bands appearing in the range of 500–600 cm^{-1} and in the range of 400–500 cm^{-1}, which have been assigned to Fe—O vibrations at the tetrahedral and octahedral sites, respectively. The appearance of these two peaks confirms the formation of both tetrahedral and octahedral sites of the spinel structure in both calcination environments (**Figure 9**). Furthermore, the force constants (K) of ions that occupy the octahedral (K_O) and tetrahedral sites (K_T) are calculated by Equations (3) and (4):

$$K = 4\pi^2 c^2 \vartheta^2 m \tag{3}$$

$$m = \frac{m_{cat.} \, m_{an.}}{m_{cat.} + m_{an.}} \tag{4}$$

where ϑ is the IR vibration band, and m is the effective mass in Daltons. $m_{cat.}$ and m_{an} are the effective masses of cation and anion, respectively, and c is the speed of light. The force constant of
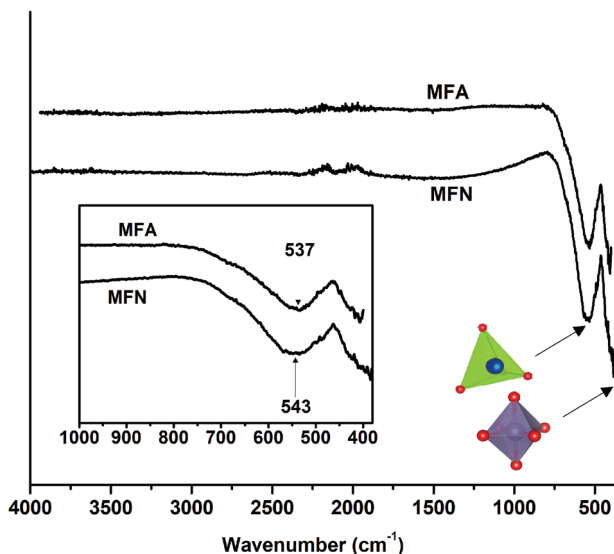
2300057 (6 of 10)

**ADVANCED
SCIENCE NEWS**

www.advancedsciencenews.com

**ADVANCED
PHYSICS
RESEARCH**
Open Access

www.advphysicsres.com

Figure 9. The FTIR spectra of MgFe$_2$O$_4$ calcined at 850 °C under Air (MFA) and Nitrogen (MFN).

the tetrahedral site is 197.0 N.cm^{-1} for MFA and 210.8 N.cm^{-1} for MFN. The low force constant of the tetrahedral site in MFA is due to less effective mass and appearance of the IR vibration band at lower wavenumbers, confirming the poor cation–anion interaction in the tetrahedral site of magnesium ferrite, by open calcination at 850 °C.

Since our instrument can measure the electrical properties of ceramics undergoing any or no surface reactions, it can be used to study those surface reactions and the electron transport in ceramics at the same time or separately. Electrical properties of MgFe$_2$O$_4$ in the temperature range of 150–250 °C have been evaluated to explore the mechanism of electron transport (**Figure 10**).

Three models, including i) simple thermal excitation, ii) small polaron hopping, and iii) 3D variable range hopping (3d-VRH), are considered to evaluate the charge transport in the MgFe$_2$O$_4$ structure. The first two models are known to have temperature-independent activation energy, while the last model is known to have temperature-dependent activation energy. The activation energy of the electron hopping is extracted from the slope of the linear fit of ln(σ) versus reciprocal temperature, based on Equation (5), if the hopping mechanism follows a simple thermal excitation model[30]:

$$\sigma = \sigma_0 \exp\left(-\frac{E_a}{k_B T}\right) \tag{5}$$

The activation energy of the electron hopping is extracted from the slope of the linear fit of ln(σT) versus the reciprocal temperature, based on Equation (6). If the hopping mechanism follows the small polaron hopping model supporting the formation of localized electrons, the equation is of the form:

$$\sigma = \frac{\sigma_0}{T} \exp\left(-\frac{E_a}{k_B T}\right) \tag{6}$$

where σ is the electrical conductivity, which is the inverse value of resistance (R), σ_0 is the pre-exponential factor, k_B is the Boltz-

mann constant, and E_a is the electron hopping activation energy, also known as the electronic bandgap.[10]

If localized electrons hop beyond the nearest neighbor center, then the hopping activation energy will be temperature-dependent.[31] Mott's Variable Range Hopping (VRH) model is due to localized energy states[32,33]:

$$\sigma\,(T) = \frac{\sigma_0}{T^{1/2}} \times \exp\left\{-\left(\frac{T_0}{T}\right)^p\right\} \tag{7}$$

where p is 1/2, 1/3, and 1/4 for 1, 2, and 3D hopping, respectively. The characteristic temperature (T_0) is related to the activation energy.[19]

The electrical conductivities of both nitrogen- and air-treated MFN are larger than those of MFA (Figure 10), for two main reasons: i) The decreased hopping length in densified magnesium ferrite spinel. The porosity of MFN, 21.5% (Table 2), is almost half the porosity of MFA, which is 42.4%. ii) The MgFe$_2$O$_4$ phase of MFA is Fe-deficient due to the formation of Fe$_2$O$_3$. Iron plays the main role in electron transfer; hence an iron deficiency harms electrical conductivity.

The electrical conductivity of MgFe$_2$O$_4$ is increased in both MFA and MFN by post-calcination treatment in an oxygen-free environment. The most energetically favored electron hopping occurs when the sample is calcined in a nitrogen atmosphere at 850 °C and is further treated under nitrogen at 250 °C. Hence, a strong Fe 3d-O 2p orbital overlap and electron exchange interaction can be achieved in such a condensed structure. The high charge density of MgFe$_2$O$_{4-x}$ was achievable by large numbers of oxygen deficiencies quantified via XPS and reported in the form of an oxygen valence of -1.4 in our previous study (Figure 10).[34]

The weighted Residual Sum of Squares (RSS) linear fit is used to evaluate the best model describing the effect of calcination and the post-calcination environment on the electron hopping mechanism through MgFe$_2$O$_4$. The low RSS value demonstrates the applicability of the model. The RSS value of the thermal excitation model decreases to almost zero when the calcination environment is changed from air to nitrogen. The RSS was then increased by further treatment of MFN under a nitrogen atmosphere. Among the three models, the 3d-VRH model fits best for MFA/Air and MFN/N$_2$; it describes the way that electron hopping of a single phase MgFe$_2$O$_4$ follows the thermal excitation model but deviates from the 3d-VRH model by either iron deficiency or oxygen deficiency (Figure 10d).

By applying the variable range electron hopping energy barrier to describe the electron transportation, the hopping energy barrier for iron-deficient and oxygen-deficient ferrites can be plotted versus temperature according to:

$$E_a\,(T) = \frac{1}{4}\,k_B T^{\frac{3}{4}} T_0^{\frac{1}{4}} \tag{8}$$

where the characteristic temperature (T_0) is extracted from Equation (7). Hence, the hopping energy through ion-deficient MgFe$_2$O$_4$, in the temperature range of 423–473 K is as plotted in **Figure 11**, which is increasing by increasing temperature for ionic deficient ferrites. Variable range electron hopping at higher temperatures (423–473 K) has not been reported for cubic
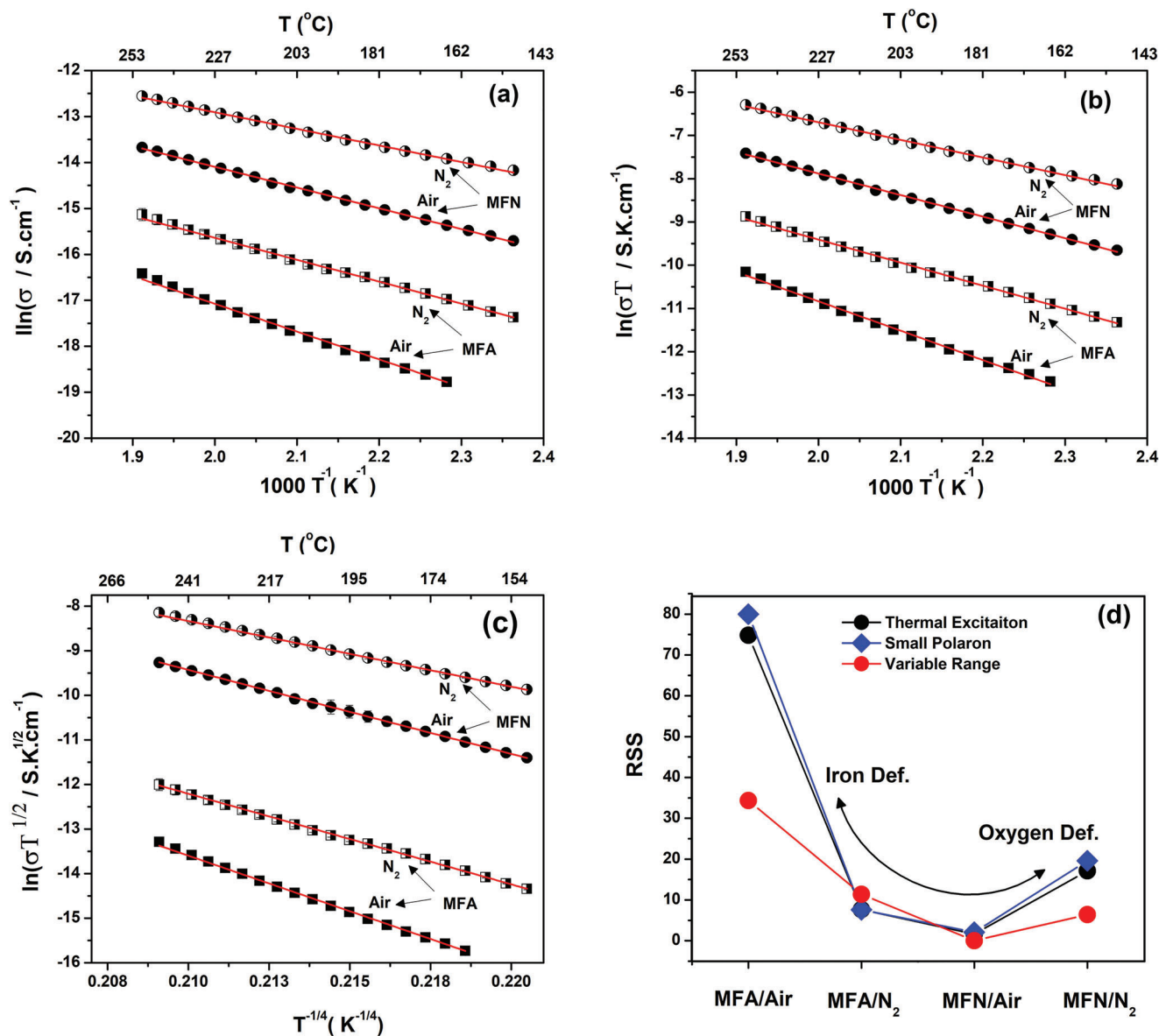
Figure 10. Plot of $\ln(\sigma)$ versus $1000/T$, a): based on the thermal excitation model, b): based on small polaron hopping model, c): $\ln(\sigma T^{1/2})$ plotted versus $1/(T^{1/4})$ based on thermal excitation model, d): and the corresponding weighted Residual Sum of Square (RSS) of the fits.

ferrites due to ionic deficiencies but was observed in non-cubic structures.[3,35]

The energy barrier of electrical hopping through iron-deficient $MgFe_2O_4$ becomes temperature-dependent due to localized electrons and structural distortions. The same behavior is observed in oxygen-deficient $MgFe_2O_4$. This is likely due to structural distortion from the introduction of nonstoichiometric spinels caused by high ionic deficiency, leading to an energy preference for a longer hopping distance. The electron hopping of cubic magnesium ferrite covers a wide energy barrier range between 0.3 and 0.6 eV, based on the calcination and post-calcination environment. The preexponential factor (σ_0) depends on the hopping probability, which is dictated by how many edge-sharing octahedral neighbors of $Fe^{2+}O_6$ are $Fe^{3+}O_6$.[19] By post-calcination treatment of both MFA and MFN under nitrogen, the concentration

of Fe^{3+} in octahedral sites is reduced, also reducing the hopping probability and σ_0 factor.

4. Conclusion

We have developed an instrument capable of observing both chemical transformation on ceramic surfaces and in situ electrical impacts of any ionic deficiency in the forms of either cationic or anionic vacancies. This novel instrument was designed with many practical features, specifically the accurate constant oxygen content of the environment while measuring electrical conductivity at high temperatures. Overall, full control of the sample cell environmental conditions was achieved, accomplished via selected gas exposures, and flexible in functionality for a wide range of possible experiments measuring redox kinetics on surfaces.
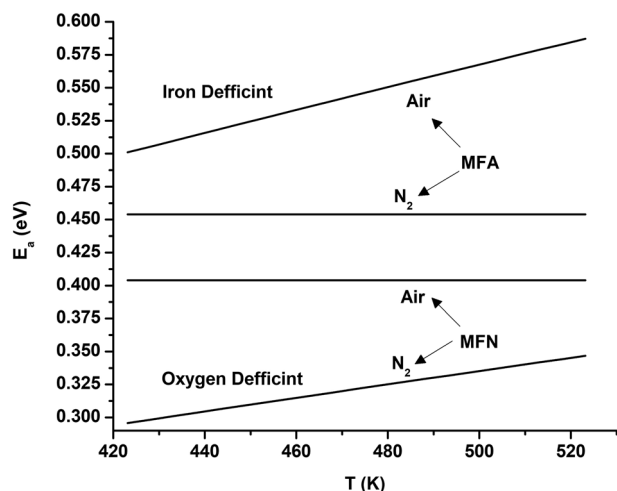
Figure 11. The activation energy (eV) according to the thermal excitation and 3D range electron hopping models.

There is seemingly no comparable instrument capable of this level of experimental customizability in combination with the described electrical and chemical measurements. Thus, a novel and practical instrumentation has been designed and successfully fabricated and used for the conclusions drawn in this report.

The results for various spinel experiments are reported here. Such measurements can be very insightful. For example, we observed the significant influence of both calcination and the post-calcination atmosphere on structural and electrical properties. The activation energy of the electron hopping in $MgFe_2O_4$, calcined at 850 °C, varies significantly in the range of ≈ 0.3–0.6 eV, depending on the calcination and post-calcination atmosphere. Cation–anion electron exchange plays a crucial role in electron hopping via double-exchange interactions, through octahedral sites of the ferrite spinels. The oxygen-free environment at the calcination stage, followed by post-calcination treatment, increases the electrical conductivity of $MgFe_2O_4$. The absence of oxygen in the atmosphere increases structural densification as well as structural negative strain. This atmospheric control is enabled by a gas system, with the additional option of liquid injection. The move of anionic oxygen toward iron cations in an octahedral site assists the electron hopping by reducing the activation energy. A simple thermal excitation model applies to $MgFe_2O_4$; however, deficiencies of iron and oxygen cause a decrease in the activation energy of electron hopping with temperature.

Acknowledgements

Conflict of Interest

The authors declare no conflict of interest.

[1] H. H. Hamdeh, J. Ho, S. A. Oliver, R. J. Willey, G. Oliveri, G. Busca, *J. Appl. Phys.* **1997**, *81*, 1851.

[2] G. Xian, S. Kong, Q. Li, G. Zhang, N. Zhou, H. Du, L. Niu, *Front. Chem.* **2020**, *8*, 177.

[3] H. A. Javar, H. Mahmoudi-Moghaddam, Z. Garkani-Nejad, G. Dehghannoudeh, *Measurement* **2022**, *191*, 110790.

[4] F. A. Benko, F. P. Koffyberg, *Mater. Res. Bull.* **1986**, *21*, 1183.

[5] J. George, K.E. Abraham *Phys. B* **2021**, *610*, 412958.

[6] P. P. Mondal, P. L. Mahapatra, S. Das, D. Saha, *Measurement* **2020**, *163*, 107992.

[7] S. R. Patade, D. D. Andhare, M. V. Khedkar, S. A. Jadhav, K. M. Jadhav, *J. Mater. Sci.: Mater. Electron.* **2021**, *32*, 13685.

[8] J. Ma, B. Zhao, H. Xiang, F. Z. Dai, Y. Liu, R. Zhang, Y. Zhou, *J. Adv. Ceram.* **2022**, *11*, 754.

[9] M. Kachniarz, J. Salach, *Measurement* **2021**, *168*, 108301.

[10] A. Bloesser, H. Kurz, J. Timm, F. Wittkamp, C. Simon, S. Hayama, B. Weber, U. P. Apfel, R. Marschall, *ACS Appl. Nano Mater.* **2020**, *3*, 11587.

[11] B. Lavina, G. Salviulo, A. D. Giusta, *Phys. Chem. Miner.* **2002**, *29*, 10.

[12] K. E. Sickafus, J. M. Wills, N. W. Grimes, *J. Am. Ceram. Soc.* **1999**, *82*, 3279.

[13] J.-G. Paik, M.-J. Lee, S.-H. Hyun, M.-J. Lee, *Thermochim. Acta* **2005**, *425*, 131.

[14] J. Guo, L. Shi, L. Wu, S. Pan, X. Yuan, J. Zhao, *Mater. Res. Express* **2018**, *5*, 126301.

[15] J. Cuenca, K. Bugler, S. Taylor, D. Morgan, P. Williams, J. Bauer, A. Porch, *J. Phys.: Condens. Matter* **2016**, *28*, 106002.

[16] J. van den Brink, D. I. Khomskii, *J. Phys.: Condens. Matter* **2008**, *20*, 434217.

[17] K. F. Wang, J.-M. Liu, Z. F. Ren, J.-M. Liu, *Adv. Phys.* **2009**, *58*, 321.

[18] L. Fu, L. Chen, K. Wang, X. Wang, *J. Alloys Compd.* **2022**, *891*, 161925.

[19] A. Bhargava, R. Eppstein, J. Sun, M. A. Smeaton, H. Paik, L. F. Kourkoutis, D. G. Schlom, M. C. Toroker, R. D. Robinson, *Adv. Mater.* **2020**, *32*, 2004490.

[20] R. Ranga, A. Kumar, P. Kumari, P. Singh, V. Madaan, K. Kumar, *Mater. Charact.* **2021**, *178*, 111269.

[21] L. I. Granone, R. Dillert, P. Heitjans, D. W. Bahnemann, *ChemistrySelect* **2019**, *4*, 1232.

[22] J. Nell, B. J. Wood, *Am. Mineral.* **1991**, *76*, 405.

[23] M. Zulqarnain, S. S. Ali, U. Hira, J. F. Feng, M. I. Khan, M. Rizwan, K. Javed, G. Farid, M. S. Hasan, *J. Alloys Compd.* **2022**, *894*, 162431.

[24] J. Podwórny, *Solid State Phenom.* **2013**, *203*, 129.

[25] H. S. C. O'Neill, A. Navrotsky, *Am. Mineral.* **1983**, *68*, 181.

[26] F. Farshidfar, A. Fattahi, R. Brüning, D. H. Ryan, K. Ghandi, *J. Adv. Ceram.* **2023**, *12*, 1612.

[27] J. P. Dhal, S. K. Sahoo, B. G. Mishra, G. Hota, *Mater. Lett.* **2017**, *196*, 95.

[28] M. Gateshki, V. Petkov, S. K. Pradhan, T. Vogt, *J. Appl. Crystallogr.* **2005**, *38*, 772.

[29] E. F. Bertaut, *J. Phys. Radium* **1951**, *12*, 252.

[30] E. Verwey, P. Haayman, F. C. Romeijn, *J. Chem. Phys.* **1947**, *15*, 181.

[31] W. Hizi, H. Rahmouni, M. Gassoumi, K. Khirouni, S. Dhahri, *Eur. Phys. J.* **2020**, *135*, 456.

[32] I. Austin, N. F. Mott, *Adv. Phys.* **1969**, *18*, 41.

[33] R. A. Sutar, L. Kumari, M. V. Murugendrappa, *J. Phys. Chem. C* **2020**, *124*, 21772.

[34] F. Farshidfar, A. Fattahi, R. Brüning, D. H. Ryan, K. Ghandi, *J. Adv. Ceram.* **2023**, *12*, 1612.

[35] M. Rudra, H. S. Tripathi, A. Dutta, T. P. Sinha, *Mat. Chem. and Phys.* **2021**, *258*, 123907.